CHEMISTRY OF MATERIALS
Cite This: Chem. Mater. 2019, 31, 9875−9886
Article
pubs.acs.org/cm

High-Quality Dual-Plasmonic Au@$Cu_{2-x}Se$ Nanocrescents with Precise $Cu_{2-x}Se$ Domain Size Control and Tunable Optical Properties in the Second Near-Infrared Biowindow

Beibei Shan,[†] Yawen Zhao,[‡] Yiwen Li,[§] Haitao Wang,[†] Rui Chen,*[,§] and Ming Li*[,†]

[†]School of Materials Science and Engineering, Central South University, Changsha, Hunan 410083, China
[‡]China Academy of Engineering Physics, Mianyang 621900, China
[§]Department of Electrical and Electronic Engineering, Southern University of Science and Technology, Shenzhen, Guangdong 518055, China

Supporting Information

ABSTRACT: Dual-plasmonic Au−$Cu_{2-x}E$ ($x > 0$, E = S, Se, Te) hybrids present multifunctionalities for broad applications in photovoltaics, photocatalysis, and biomedicine. However, despite the increasing interest in these dual-plasmonic Au−$Cu_{2-x}E$ hybrids, precise control over the morphology and size of their substituents is crucial but greatly challenging. Herein, a selenium-mediated two-step synthetic approach is developed to prepare the Au@$Cu_{2-x}Se$ nanocrescents with precise control over their size and tunable plasmonic properties through varying the concentration of the SeO_2 precursor. The complete encapsulation of the Au domain within the $Cu_{2-x}Se$ layer in the nanocrescent in an asymmetric manner enables the strong coupling between their substituents, significantly enhancing their optical properties supported by both experimental results and theoretical modeling. The increasing $Cu_{2-x}Se$ domain size enables the tuning of carrier densities and thereby molar extinction coefficients corresponding to the respective visible and near-infrared (NIR) plasmon bands of the Au@$Cu_{2-x}Se$ nanocrescents. Electron transfer from the Au to $Cu_{2-x}Se$ domains is unambiguously determined in the Au@$Cu_{2-x}Se$ nanocrescents by transient absorption (TA) and extinction spectral measurements. The $Cu_{2-x}Se$-dependent bleaching amplitude and carrier dynamics of both visible and NIR plasmon TA signals are observed, along with variations of the carrier−phonon and phonon−phonon relaxation processes. This work not only presents a facile synthetic approach of high-quality dual-plasmonic Au@$Cu_{2-x}Se$ nanocrescents and a fundamental understanding of the coupling mechanism in the Au−$Cu_{2-x}Se$ hybrid system, but also provides a paradigm for the study on the interplay in a dual-plasmonic metal−semiconductor system.

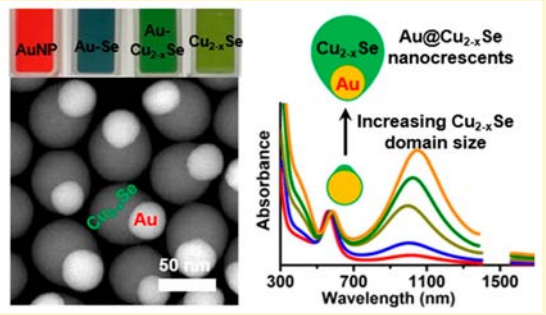

INTRODUCTION

Plasmonic materials find a plethora of applications ranging from photovoltaics and light-driven catalysis to biomedicine such as biosensing, bioimaging, and cancer theranostics.[1−4] Noble metals and nonstoichiometric copper chalcogenides ($Cu_{2-x}E$, $x > 0$, E = S, Se, Te) are among the most studied plasmonic materials and have been extensively exploited as building blocks of multifunctional materials for those plasmon-based applications.[5−9] Au and Ag are the most commonly used plasmonic noble metals, whose surface plasmon resonances (SPRs) mainly arise from the collective oscillation of their free conduction electrons driven by the electromagnetic field of incident light.[5,10] The large intrinsic free carrier (electron) density (~10^{23} cm^{-3}) in noble metals makes their SPR bands in the visible (400−700 nm) and first near-infrared (NIR-I, 700−900 nm) regions;[11] the plasmonic response of these noble metals strongly depends on their composition, particle size, and geometric shape, and the dielectric function of the surrounding environments.[2,12−14] Although tailoring the anisotropic shape (i.e., nanorods, nanocages, hollow spheres, and core−shells) allows for tuning the SPR band of noble metal nanostructures into the second NIR biowindow (NIR-II, 1000−1350 nm) favorable for in vivo biomedical applications, both large particle size of >100 nm and high power density exceeding the maximum laser permissible exposure (0.33 W/cm^2 for 808 nm laser, 1.0 W/cm^2 for 1064 nm laser) restrict their in vivo bioapplications.[15−17] Nonstoichiometric copper chalcogenides are a novel class of p-type semiconducting materials with characteristic SPR bands in the NIR spectral region especially in the NIR-II transparent biowindow. Unlike noble metals, their plasmons are supported by the positively charged holes as a result of the Cu vacancy, with a carrier density of 10^{19}−10^{21} cm^{-3} relatively lower than noble metals.[18,19] The SPR band of $Cu_{2-x}E$ can be effectively

Received: October 7, 2019
Revised: November 13, 2019
Published: November 13, 2019

DOI: 10.1021/acs.chemmater.9b04100
Chem. Mater. 2019, 31, 9875−9886

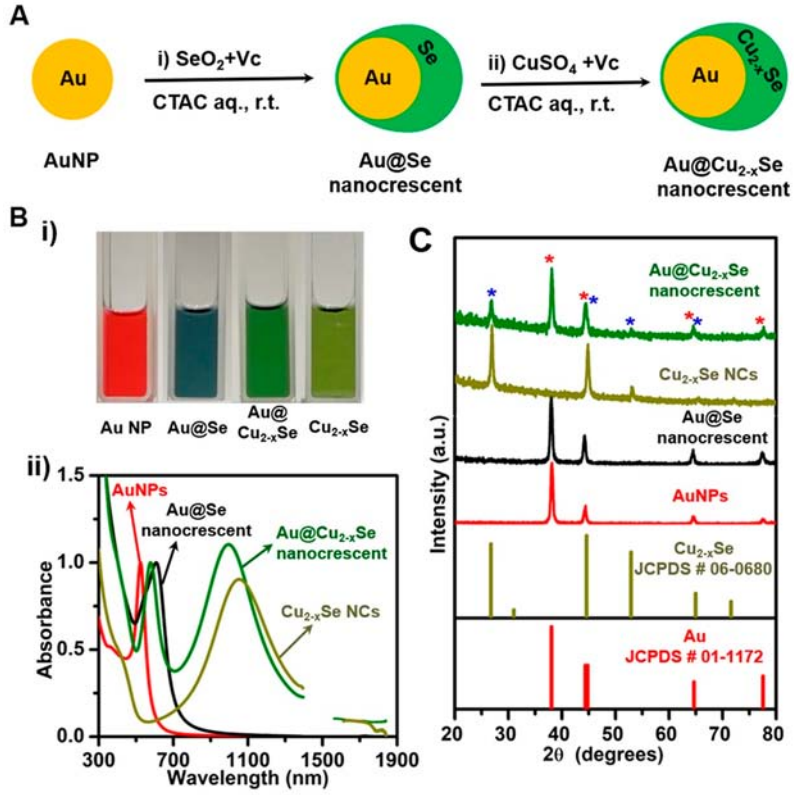

Figure 1. Synthesis and characterization of Au@Cu_{2-x}Se nanocrescents by a Se-mediated two-step process. (A) Schematic illustrating the synthesis process of Au@Cu_{2-x}Se nanocrescents by a Se-mediated two-step process: (i) the selenium layer was first coated onto the AuNPs by the reduction of SeO_2 using Vc as the reducing agent, yielding the Au@Se nanocrescents, and then (ii) the selenium layer was converted to Cu_{2-x}Se, producing the Au@Cu_{2-x}Se nanocrescents in the presence of copper(II), CTAC, and Vc. (B) (i) Optical image and (ii) optical extinction spectra of aqueous solutions of AuNPs, Cu_{2-x}Se NCs, Au@Se nanocrescents, and Au@Cu_{2-x}Se nanocrescents. The spikes arising from the strong absorption of water medium in the ∼1410−1550 nm range of the extinction spectra were removed. The Au@Se nanocrescents were synthesized with 1.00 mM SeO_2, followed by the conversion into Au@Cu_{2-x}Se nanocrescents. (C) Powder XRD patterns of AuNPs, Cu_{2-x}Se NCs, Au@Se nanocrescents, and Au@Cu_{2-x}Se nanocrescents. The standard XRD patterns of Au and Cu_{2-x}Se are shown as well for reference and comparison (JCPDS no. 01-1172 of cubic Au; JCPDS no. 06-0680 of cubic berzelianite Cu_{2-x}Se).

tuned by varying the degree of the Cu vacancy. Moreover, the plasmonic properties of Cu_{2-x}E can be postsynthetically modulated by chemically doping or electrochemically charging and discharging, a unique feature different from the classical metal plasmonics.[20−22]

Considerable efforts have been made to develop noble metal−semiconductor hybrids that combine the respective merits of their constituents to synergistically enhance their performances in surface-enhanced spectroscopies, biosensing, bioimaging, and cancer photothermal therapy.[23−31] The interest in such dual-plasmonic hybrids is mainly driven by the electronic interactions that modulate the energy transfer and local plasmonic field. The combination of two entirely different types of plasmonic materials such as noble metals and semiconductors could also yield new unexpected phenomena due to the interaction of two intrinsically dissimilar plasmonic building blocks. Previous studies showed that the combination of Au and Cu_{2-x}E greatly improved the visible and NIR absorption through the strong plasmonic coupling between the Au and Cu_{2-x}E domains, and simultaneously preserved a small size (<50 nm) suitable for the efficient cell internalization along with prolonging in vivo circulation.[26,31−34] More importantly, the dual-plasmonic system of Au and Cu_{2-x}E presents multiple functionalities for promising multimodality diagnostics and therapy of cancer, for example, integrating surface-enhanced Raman spectroscopy (SERS), photoacoustic imaging, and X-ray computed tomography in a single system for diagnostics,[23,32] along with photothermal therapy and photodynamic therapy for cancer therapy.[35,36] However, despite intensive efforts, few reports are dedicated to elucidate the interplay between the free electron- and free hole-based plasmons in the Au and Cu_{2-x}E domains of the Au−Cu_{2-x}E hybrids, respectively. Previous studies showed that the plasmonic coupling caused the red-shift of the Au-associated plasmon band and the blue-shift of the Cu_{2-x}Se-associated plasmon band in the Au@Cu_{2-x}Se core−shell structures with respect to the plasmon bands of Au nanoparticles (AuNPs) and Cu_{2-x}Se nanoparticles only.[23,32] Because of the synergistic interactions, the optical properties of the Au−Cu_{2-x}Se hybrids are not simply the sum of those of the Au and Cu_{2-x}Se constituents. The influence of the refractive index, plasmonic coupling, charge redistribution, and others could intertwine together to account for the unique plasmonic properties in such a dual-plasmonic Au−Cu_{2-x}Se system. A systematic study for the in-depth understanding of the interplay of the Au and the Cu_{2-x}E domains in the Au−Cu_{2-x}E hybrids becomes greatly crucial but is still lacking.

Here, we developed a selenium-mediated two-step synthetic approach to prepare the dual-plasmonic Au@Cu_{2-x}Se nanocrescents with tunable Cu_{2-x}Se domain size and NIR

DOI: 10.1021/acs.chemmater.9b04100
Chem. Mater. 2019, 31, 9875−9886

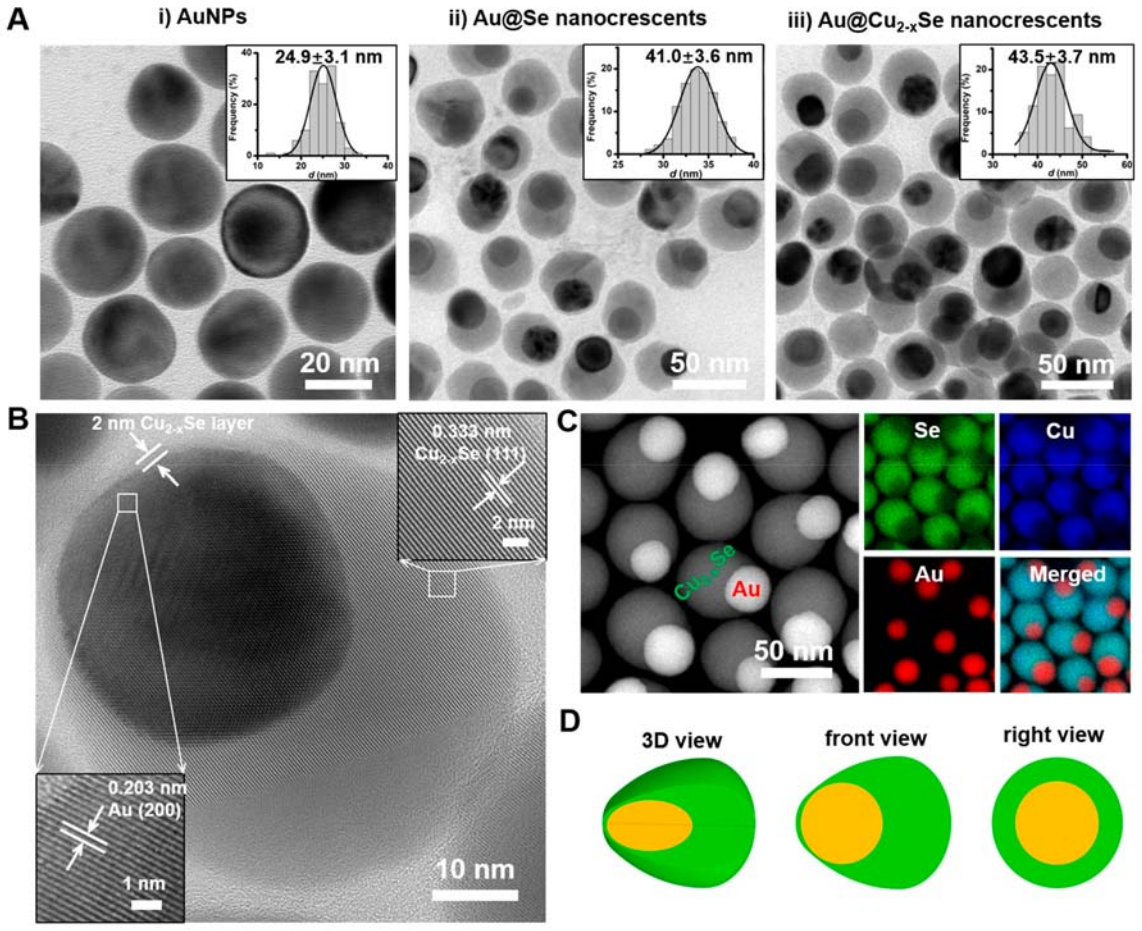

Figure 2. Morphology, size, and compositional distributions of AuNPs, Au@Se nanocrescents, and Au@Cu_{2-x}Se nanocrescents. (A) TEM images and size distribution (inset) of (i) AuNPs, (ii) Au@Se nanocrescents, and (iii) Au@Cu_{2-x}Se nanocrescents. The size of Au@Se nanocrescents and Au@Cu_{2-x}Se nanocrescents is the total size in the largest dimension of the nanoparticles containing the Au and Se or Cu_{2-x}Se domains. (B) HRTEM image of a representative Au@Cu_{2-x}Se nanocrescent. 1.0 mM SeO_2 was used for the synthesis of the Au@Cu_{2-x}Se nanocrescents. (C) HAADF-STEM and the corresponding EDX elemental mapping of the Au@Cu_{2-x}Se nanocrescent. 2.0 mM SeO_2 was used for the synthesis of the Au@Cu_{2-x}Se nanocrescents. (D) A schematic model illustrating the three-dimensional structure of the Au@Cu_{2-x}Se nanocrescent.

plasmonic properties. The Cu_{2-x}Se domain size of the nanocrescents was precisely controlled by varying the concentration of the SeO_2 precursor. The increasing Cu_{2-x}Se domain size is able to modulate the interactions between the Au and Cu_{2-x}Se domains in the Au@Cu_{2-x}Se nanocrescents and their optical properties accordingly. Unlike previous studies on the Au−Cu_{2-x}Se dimers where the interfacial contact area is partial,[23,26,37] the complete encapsulation of the Au domain within the Cu_{2-x}Se in the present nanocrescent structures enables an intimate contact over a larger surface area without native Au surface exposure and thus excludes the unnecessary interference from the external environment. The asymmetric geometry of the nanocrescents yields the asymmetric electric field distribution along the Au−Cu_{2-x}Se interface and the nanocrescent surface, which is responsible for the unique plasmonic properties. We employed the theoretical modeling and transient absorption (TA) measurements to understand the evolution of plasmonic properties of the Au@Cu_{2-x}Se nanocrescents with the Cu_{2-x}Se domain size and elucidate the physics of the interplay between their Au and Cu_{2-x}Se domains. Results show that the electron transfer from the Au domain to the Cu_{2-x}Se domain accounts for their strong coupling interactions, modulating the carrier−phonon scattering and phonon−phonon relaxation processes. Our findings unambiguously reveal the underlying physics of the strong coupling of the Au domain with the Cu_{2-x}Se domain in the hybrids, and provide a guidance for designing dual-plasmonic metal−semiconductor nanostructures with optimal NIR optical performances.

RESULTS AND DISCUSSION

Dual-plasmonic Au@Cu_{2-x}Se nanocrescents were synthesized by a selenium-mediated two-step process:[31] (i) the direct synthesis of Au@Se nanocrescents and (ii) the subsequent conversion into the Au@Cu_{2-x}Se nanocrescents (Figure 1A). First, the hexadecyltrimethylammonium chloride (CTAC)-stabilized AuNPs were coated with an amorphous Se layer through the reduction of SeO_2 by the ascorbic acid (Vitamin C, Vc) reducing agent, forming the Au@Se nanocrescent structure. This synthetic method is mainly inspired by the high affinity of the Au surface toward the elemental Se and selenides, which has been widely exploited for synthesis of Au-chalcogenide core−shell NPs with large lattice mismatch.[38,39] It should be noted that the CTAC stabilizer is critical for forming the Au@Se nanocrescent structure. The resulting Au@Se nanocrescents then were further reacted with Cu^{2+} in an aqueous solution of CTAC and Vc, yielding the Au@

DOI: 10.1021/acs.chemmater.9b04100
Chem. Mater. 2019, 31, 9875−9886

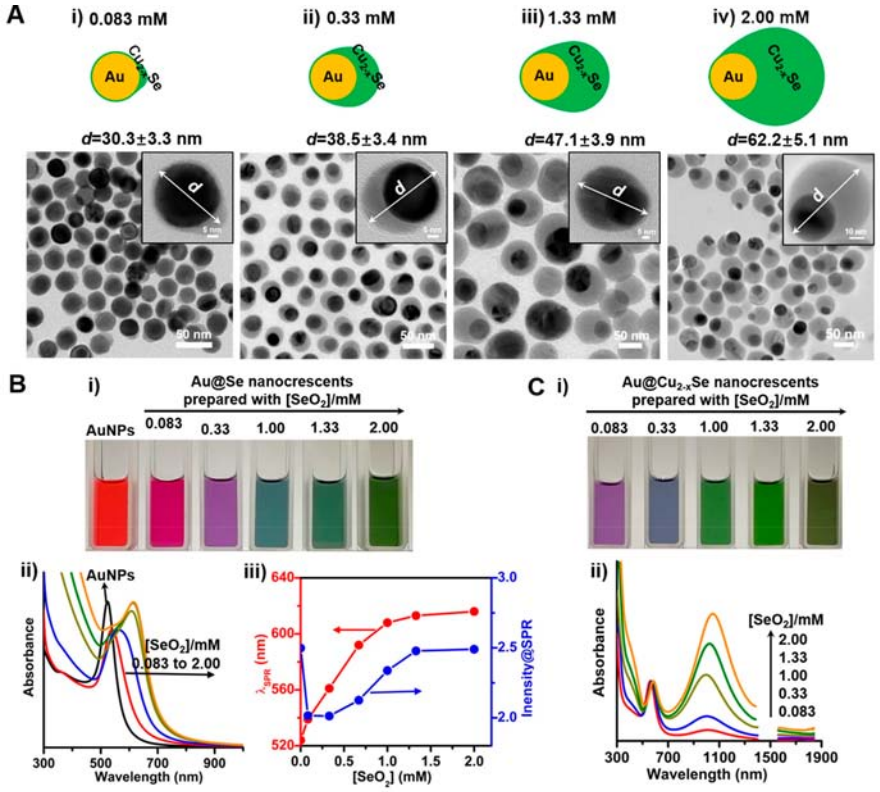

Figure 3. Evolution of the $Cu_{2-x}Se$ domain size and optical properties with varying SeO_2 concentration of Au@$Cu_{2-x}Se$ nanocrescents. (A) TEM images (bottom) and their corresponding schematic structures (top) of Au@$Cu_{2-x}Se$ nanocrescents synthesized with the SeO_2 concentration of (i) 0.083 mM, (ii) 0.33 mM, (iii) 1.33 mM, and (iv) 2.00 mM. The insets in the panels (A(i–iv)) are the TEM images of a representative Au@$Cu_{2-x}Se$ nanocrescent for the corresponding SeO_2 concentration, and the arrow indicates the size representing the largest dimension of the nanocrescent in their TEM images. The average size statistically obtained from the corresponding TEM images was shown as well. (B) (i) Optical image and (ii) extinction spectra of aqueous solutions of AuNPs and Au@Se nanocrescents synthesized with various SeO_2 concentrations (0.083, 0.33, 1.00, 1.33, and 2.00 mM), and (iii) plot of both SPR wavelength and extinction intensity at the SPR wavelength as a function of the SeO_2 concentration. (C) (i) Optical image and (ii) extinction spectra of aqueous solutions of Au@$Cu_{2-x}Se$ nanocrescents obtained from the conversion of Au@Se nanocrescents shown in (B). The spikes arising from the strong absorption of water medium in the ~1410–1550 nm range of the extinction spectra were removed.

$Cu_{2-x}Se$ nanocrescents. Cu^{2+} was reduced to Cu^{+} by the weak Vc reducing agent, and then reacted with the elemental Se to produce the Cu-deficient $Cu_{2-x}Se$ upon the exposure to air for oxidation. The initial amorphous Se layer on the AuNP surface as the template facilitates the high control of the $Cu_{2-x}Se$ coating onto the AuNP surface because of the large lattice mismatch between AuNPs and $Cu_{2-x}Se$ crystals.

A wine red-to-cyan color change was accomplished immediately after SeO_2 was added to the AuNP suspension containing the Vc; the reaction solution became dark green along with the conversion of the Au@Se nanocrescents into the Au@$Cu_{2-x}Se$ nanocrescents, also reflected by the spectral variation of their extinction spectra (Figure 1B(ii)). The characteristic SPR peak of the AuNPs red-shifts from 524 to 608 nm after the Se layer coating, which is ascribed to the higher refractive index (n > 2.70 at 524–608 nm) of Se than that (n = 1.33) of the water medium.[40,41] The optical extinction spectrum of Au@$Cu_{2-x}Se$ nanocrescents made with 1.0 mM SeO_2 shows two characteristic peaks at 578 and 996 nm, which are assigned to the SPR bands corresponding to its Au and $Cu_{2-x}Se$ domains, respectively. A blue-shift by 30 nm (from 608 to 578 nm) is observed for the Au-associated SPR band along with the conversion of the Au@Se to Au@$Cu_{2-x}Se$ nanocrescents (Figure 1B(ii)). Three intertwined factors that are the refractive index change (n = 2.6 for $Cu_{2-x}Se$; n < 1 for Au at >500 nm), charge redistribution, and plasmonic coupling effects may be responsible for the red-shift of the Au-associated SPR band and the blue-shift of the $Cu_{2-x}Se$-associated SPR band in Au@$Cu_{2-x}Se$ nanocrescents with respect to the SPR bands of AuNPs and $Cu_{2-x}Se$ nanocrystals (NCs), respectively. The powder XRD result confirms the amorphous form of the Se layer on the AuNP surface (Figure 1C). In the Au@$Cu_{2-x}Se$ nanocrescents, characteristic 2θ peaks at 26.7°, 44.6°, 52.9°, and 64.9° all can be indexed to the cubic berzelianite structure of $Cu_{2-x}Se$ (JCPDS no. 06-0680 of cubic berzelianite $Cu_{2-x}Se$), while the 2θ peaks at 38.1° and 77.5° are attributed to the cubic Au structure (JCPDS no. 01-1172 of cubic Au). We also synthesized the $Cu_{2-x}Se$ NCs (33.8 ± 1.9 nm) in the absence of AuNPs, showing the same cubic berzelianite structure as the Au@$Cu_{2-x}Se$ nanocrescents (Figures 1C and S3). Thus, the XRD patterns confirm the successful synthesis of highly crystalline Au@$Cu_{2-x}Se$ nanocrescrents.

The TEM image clearly confirms the coating of the Se layer on the spherical AuNPs, forming the Au@Se nanocrescent structure (Figure 2A). In the nanocrescent structure, the AuNP domain appearing in much darker contrast was completely encapsulated by a lighter $Cu_{2-x}Se$ layer because of their different atomic numbers. The conversion of the amorphous Se into crystalline $Cu_{2-x}Se$ preserves the initial nanocrescent morphology but causes a slight (~2 nm) increase

DOI: 10.1021/acs.chemmater.9b04100
Chem. Mater. 2019, 31, 9875–9886

Table 1. Summary of Optical Properties, x Value, and Carrier Density of AuNPs, $Cu_{2-x}Se$ NCs, and Au@$Cu_{2-x}Se$ Nanocrescents Synthesized with Various SeO_2 Concentrations

sample	[SeO_2] (mM)	$N(Cu_{2-x}Se):N(Au)$[a]	x value[b]	λ_{max}(Au) (nm)	ε(Au)[c] $(M\ cm)^{-1}$	N_e (cm^{-3})[d]	$\lambda_{max}(Cu_{2-x}Se)$ (nm)	$\varepsilon(Cu_{2-x}Se)$[c] $(M\ cm)^{-1}$	N_h (cm^{-3})[d]
AuNPs	0	0	N/A	524	8.57×10^9	1.87×10^{22}	NA	NA	NA
Au@$Cu_{2-x}Se$-1	0.083	0.18	0.20	560	2.18×10^9	1.68×10^{22}	1011	8.47×10^7	4.45×10^{21}
Au@$Cu_{2-x}Se$-2	0.33	0.71	0.19	571	3.25×10^9	1.60×10^{22}	1002	9.25×10^8	4.37×10^{21}
Au@$Cu_{2-x}Se$-3	1.00	1.96	0.19	578	3.00×10^9	1.58×10^{22}	996	2.37×10^9	4.30×10^{21}
Au@$Cu_{2-x}Se$-4	1.33	2.42	0.20	579	3.46×10^9	1.54×10^{22}	1025	4.12×10^9	4.05×10^{21}
Au@$Cu_{2-x}Se$-5	2.00	3.77	0.19	585	3.66×10^9	1.50×10^{22}	1052	6.99×10^9	3.83×10^{21}
$Cu_{2-x}Se$ NCs	2.44	NA	0.20	NA	NA	NA	1053	1.97×10^9	4.05×10^{21}

[a]The $N(Cu_{2-x}Se):N(Au)$ ratio is the atomic ratio of the $Cu_{2-x}Se$ to Au atoms in the Au@$Cu_{2-x}Se$ nanocrescents estimated by ICP-OES. [b]The x value was estimated by ICP-OES. [c]The molar extinction coefficients (ε(Au) and $\varepsilon(Cu_{2-x}Se)$) correspond to the SPR wavelengths λ_{max}(Au) and $\lambda_{max}(Cu_{2-x}Se)$ associated with the Au and $Cu_{2-x}Se$ domains, respectively. [d]N_e and N_h represent free electron and free hole densities estimated on the basis of the SPR bands corresponding to the Au and $Cu_{2-x}Se$ domains, respectively.

of the total size due to the Cu atom incorporation (Figure 2A). The HRTEM image of a representative Au@$Cu_{2-x}Se$ nanocrescent in Figure 2B unveils the complete encapsulation of the AuNP by a $Cu_{2-x}Se$ layer of high crystallinity. The lattice fringes with the interplanar spacings of 0.333 and 0.203 nm correspond to the (111) and (200) planes of the $Cu_{2-x}Se$ and Au domains, respectively. This is consistent with the XRD results. Both HRTEM and HAADF-STEM images clearly show that the as-prepared Au@$Cu_{2-x}Se$ hybrids possess a crescent structure where the AuNP is completely encapsulated by a $Cu_{2-x}Se$ layer in an asymmetric manner. Furthermore, the STEM-EDX mapping shows a clear distribution of Cu and Se in the outer layer and Au in the dark core, confirming the crescent structure again. Therefore, all of this evidence corroborates the controllable synthesis of the high-quality dual-plasmonic Au@$Cu_{2-x}Se$ nanocrescents by the Se-mediated method.

We further probed the tunability of the Au@$Cu_{2-x}Se$ nanocrescents by varying the SeO_2 concentration from 0.083 to 2.00 mM (Figure 3). It can be clearly seen that all samples have a crescent structure and there exists a thin (~2 nm) $Cu_{2-x}Se$ layer conformally coating on the one side of the AuNP surface. The total size of the Au@$Cu_{2-x}Se$ nanocrescents is proportional to the SeO_2 concentration, and the size of the $Cu_{2-x}Se$ domain is 30.3 ± 3.3, 38.5 ± 3.4, 41.0 ± 3.6, 47.1 ± 3.9, and 62.2 ± 5.1 nm for the Au@$Cu_{2-x}Se$ nanocrescents made with the SeO_2 concentrations of 0.083, 0.33, 1.00, 1.33, and 2.00 mM, respectively (Figure S4). It is worth pointing out that $Cu_{2-x}Se$ mainly grows unidirectionally on the one side of the Au domain even with more addition of the SeO_2 precursor, forming the crescent structure. The replacement of the CTAC stabilizer with other stabilizers such as poly(vinylpyrrolidone) and poly(diallyldimethylammonium chloride) produced symmetrical core−shell or isolated nanostructures rather than the crescent-like structure. It is suggested that the shielding effect of CTAC on the deposition of Se atoms is responsible for the formation of Au@$Cu_{2-x}Se$ nanocrescents.[31] The color of the suspension of the Au@Se nanocrescents gradually evolves from red to dark green with the SeO_2 concentration increasing up to 2.00 mM, while the Au@$Cu_{2-x}Se$ nanocrescents appear violet to dark green accordingly (Figure 3B,C). The UV−vis−NIR extinction spectra show a gradual red-shift of the SPR band of the Au@Se nanocrescents with the increasing Se domain size (due to the increasing SeO_2 concentration), while the extinction intensity undergoes first a steep decrease and then a gradual increase with the increasing Se domain size. The rationale is the relatively large refractive index of Se and the lack of the electronic interactions between the Au and the amorphous Se. There exist two SPR bands associated with the Au and $Cu_{2-x}Se$ domains for all Au@$Cu_{2-x}Se$ nanocrescents; the SPR band corresponding to the $Cu_{2-x}Se$ domain is located in the NIR-II region of ca. 990−1050 nm, and the SPR band corresponding to the Au domain is in the visible region of 560−585 nm, red-shifting with respect to that of the AuNPs. The intensity of the NIR SPR band is proportional to the total size of the $Cu_{2-x}Se$ domain. We also noted the red-shift of the interband transition-induced absorption onset around 300−500 nm of $Cu_{2-x}Se$ in Au@$Cu_{2-x}Se$ nanocrescents with the increasing $Cu_{2-x}Se$ domain size, probably resulting from the quantum size effects (Figure 3C(ii)). Thus, we confirm that the size of the Au@$Cu_{2-x}Se$ nanocrescents can be effectively controlled by the initial concentration of the SeO_2 precursor, tuning their plasmonic properties accordingly. The corresponding plasmonic properties of all Au@$Cu_{2-x}Se$ nanocrescents along with those of AuNPs and $Cu_{2-x}Se$ NCs are listed in Table 1.

We analyzed the elemental composition of all as-synthesized Au@$Cu_{2-x}Se$ nanocrescents by ICP-OES, and then derived their "x" values and the molar ratios of the $Cu_{2-x}Se$ to Au atom accordingly ($N(Cu_{2-x}Se):N(Au)$, equivalent to the Se to Au atomic ratio) (Table 1). It can be seen that the $N(Cu_{2-x}Se):N(Au)$ value increases from 0.18 to 3.77 with the increasing SeO_2 concentration from 0.083 to 2.00 mM. Results show the similar x value of ~0.2 for all Au@$Cu_{2-x}Se$ nanocrescents, consistent with the literature.[21,42] Furthermore, we determined the molar extinction coefficients ($\varepsilon(\lambda)$) corresponding to the respective SPR bands of the Au and $Cu_{2-x}Se$ domains according to the Lambert−Beer law:[43]

$$A(\lambda) = \varepsilon(\lambda) \cdot l \cdot c \quad (1)$$

where $A(\lambda)$, l, and c are the optical density at the SPR wavelength (λ), the length of the solution the incident light passes through (1 cm for the standard cuvette), and the concentration of the Au and $Cu_{2-x}Se$ domains (mol/L), respectively. The atomic concentrations of Au, Cu, and Se determined by ICP-OES were converted to the particulate concentration of the Au and $Cu_{2-x}Se$ domains, whose details were shown in the Supporting Information.[43] A dramatic decrease of the molar extinction coefficient of the Au domain-associated SPR band (ε(Au)) is observed after being encapsulated with the $Cu_{2-x}Se$, followed by a monotonic and

DOI: 10.1021/acs.chemmater.9b04100
Chem. Mater. 2019, 31, 9875−9886

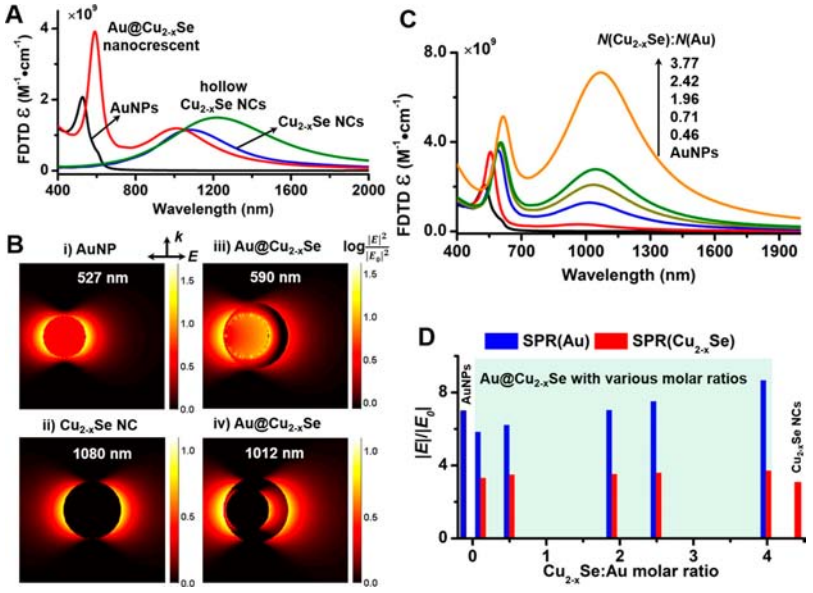

Figure 4. Theoretical analysis of plasmonic properties of Au@$Cu_{2-x}Se$ nanocrescents with various $Cu_{2-x}Se$:Au molar ratios. (A) Calculated extinction spectra of AuNPs, $Cu_{2-x}Se$ NCs, hollow $Cu_{2-x}Se$ NCs, and Au@$Cu_{2-x}Se$ nanocrescents. The AuNPs and $Cu_{2-x}Se$ NCs are, respectively, modeled as a sphere of 25 and 33.8 nm in diameter taken from Figure 2, and the sizes of the AuNP and $Cu_{2-x}Se$ domains in the nanocrescent are consistent with those of AuNPs and $Cu_{2-x}Se$ NCs. The structure of hollow $Cu_{2-x}Se$ NCs is similar to the Au@$Cu_{2-x}Se$ nanocrescent except the removal of the Au domain. (B) Distribution of electric field ($\log(|E|^2/|E_0|^2)$) of (i) AuNPs at its visible SPR wavelength (527 nm), (ii) $Cu_{2-x}Se$ NCs at its NIR SPR wavelength (1080 nm), and (iii, iv) Au@$Cu_{2-x}Se$ nanocrescents at its visible and NIR SPR wavelengths corresponding to (iii) the Au domain (590 nm) and (iv) the $Cu_{2-x}Se$ domain (1012 nm). (C) Evolution of the calculated extinction spectra of Au@$Cu_{2-x}Se$ nanocrescents with the increasing $Cu_{2-x}Se$:Au molar ratios. (D) The maximal electric field intensity ($|E|/|E_0|$) of AuNPs and $Cu_{2-x}Se$ NCs at their SPR wavelengths, and of Au@$Cu_{2-x}Se$ nanocrescents of various $Cu_{2-x}Se$:Au molar ratios at the SPR wavelengths corresponding to their Au and $Cu_{2-x}Se$ domains, respectively.

slight increase with the increasing $N(Cu_{2-x}Se):N(Au)$ value; however, we can see 1−2 orders of magnitude increase of the $\varepsilon(Cu_{2-x}Se)$ value of the Au@$Cu_{2-x}Se$ nanocrescents with the increasing $N(Cu_{2-x}Se):N(Au)$ (Table 1).

To better understand the plasmonic properties of the dual-plasmonic Au@$Cu_{2-x}Se$ nanocrescents, FDTD calculations of both extinction spectra and electric field distribution were performed for AuNPs, $Cu_{2-x}Se$ NCs, and the corresponding Au@$Cu_{2-x}Se$ nanocrescent (Figure 4A,B). The nanocrescent is modeled with an Au sphere (25 nm in diameter) asymmetrically embedded within the $Cu_{2-x}Se$ sphere (33.8 nm in diameter), as schematically shown in Figure S2. The Au and $Cu_{2-x}Se$ domains in the nanocrescent have the same size as the AuNPs and $Cu_{2-x}Se$ NCs, respectively. The calculated extinction spectrum of the Au@$Cu_{2-x}Se$ nanocrescents clearly shows two separated SPR bands located in the visible and NIR regions, associated with the Au and $Cu_{2-x}Se$ domains, respectively (Figure 4A). This is consistent with the experimental results shown in Figure 1B. The visible SPR band of the Au@$Cu_{2-x}Se$ nanocrescents red-shifts and concomitantly becomes stronger, while its NIR SPR band blue-shifts, with respect to those of AuNPs and $Cu_{2-x}Se$ NCs, respectively. Surprisingly, we also observed the enhanced NIR SPR band in the hollow $Cu_{2-x}Se$ NCs where the Au domain was removed from the Au@$Cu_{2-x}Se$ nanocrescent. We further calculated the electric field distribution and then compared their maximal electric field intensities ($|E|/|E_0|$). The asymmetric distribution of electric field was observed in the Au@$Cu_{2-x}Se$ nanocrescents; the maximal electric field corresponding to the visible or NIR SPR band appears at the left side of the $Cu_{2-x}Se$ domain, quite different from those of AuNPs and $Cu_{2-x}Se$ NCs (Figure 4A,B). A close examination reveals that the electric field is much stronger at the right side of the Au domain of the nanocrescent than that at its left side. On the basis of the average size statistically estimated from the TEM images for all Au@$Cu_{2-x}Se$ nanocrescents, we further examined the effect of the $Cu_{2-x}Se$ domain size on the electric field (Figures 4C,D, S5, and S6). Both visible and NIR SPR bands gradually red-shift and concomitantly increase in the intensity with the increasing $Cu_{2-x}Se$ domain size (Figure 4C). We can clearly see that the maximal electric field intensity at the visible SPR wavelength decreases from the AuNPs to nanocrescents, and then gradually increases with the increasing $Cu_{2-x}Se$ domain size; in contrast, all Au@$Cu_{2-x}Se$ nanocrescents exhibit the maximal electric field intensity at the NIR SPR wavelength much higher than $Cu_{2-x}Se$ NCs alone, indicating the coupling effect that enhances the NIR electric field in the Au@$Cu_{2-x}Se$ nanocrescents (Figure 4D).

According to the Drude model, we calculated the free electron (N_e) and free hole (N_h) densities corresponding to the visible and NIR SPR bands of the nanocrescents, respectively.[18,44,45]

$$\omega_{sp} = \sqrt{\frac{\omega_p^2}{\varepsilon_\infty + 2\varepsilon_m} - \gamma^2} \tag{2}$$

where ω_{sp} and γ are the frequency and full-width-at-half-maximum (fwhm) of the SPR bands, respectively; ε_∞ and ε_m are the high frequency dielectric constant and the solvent dielectric constant ($\varepsilon_m = n_m^2 = 1.33^2 = 1.77$ for water here), respectively; ω_p is the bulk plasma oscillation frequency related to the free electron or hole density. γ can be determined by fitting the SPR band to a Gaussian function, and ε_∞ can be treated as 7.0 for $Cu_{2-x}Se$ at $x = 0.2$ according to the

DOI: 10.1021/acs.chemmater.9b04100
Chem. Mater. 2019, 31, 9875−9886

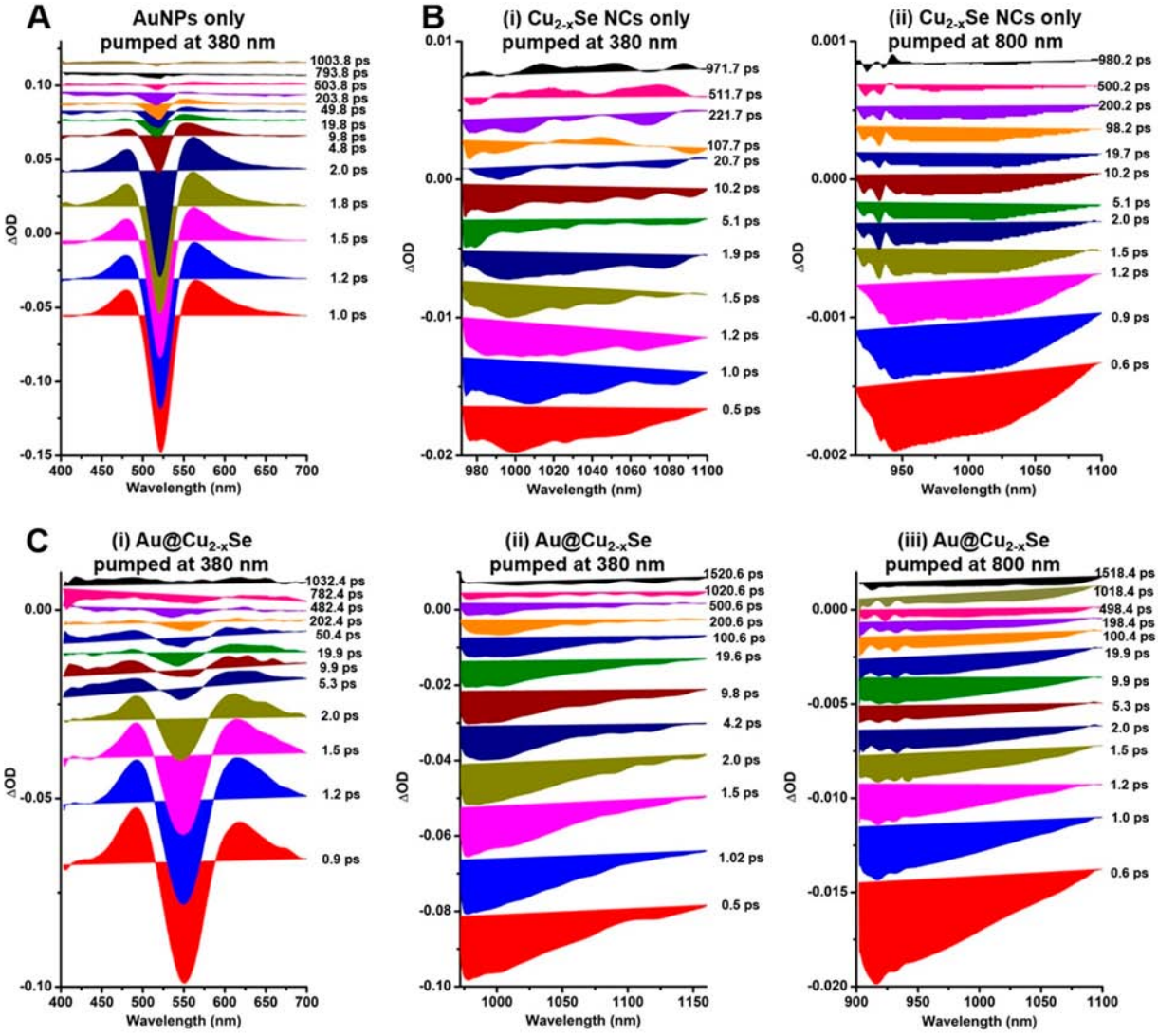

Figure 5. Transient absorption spectra of AuNPs, $Cu_{2-x}Se$ NCs, and Au@$Cu_{2-x}Se$ nanocrescents. (A) Transient absorption spectra of AuNPs in the visible region at various delay times, pumped at 380 nm. (B) Transient absorption spectra at various delay times of $Cu_{2-x}Se$ NCs (i) in the visible region pumped at 380 nm and (ii) in the NIR region pumped at 800 nm. (C) Transient absorption spectra at various delay times of Au@$Cu_{2-x}Se$ nanocrescents (i) in the visible region pumped at 380 nm, (ii) in the NIR region pumped at 380 nm, and (iii) in the NIR region pumped at 800 nm. The present Au@$Cu_{2-x}Se$ nanocrescents have a $Cu_{2-x}Se$:Au molar ratio of 0.71, which were prepared with 0.33 mM SeO_2.

literature.[46] Thus, we calculated the free carrier density (N= N_e or N_h) by the following equation:[18,44,45]

$$\omega_p^2 = \frac{Nq_e^2}{\varepsilon_0 m^*} \quad (3)$$

where m^* is the charge carrier effective mass ($m^* = m_0$ for a free electron, $m^* = 0.336m_0$ for a free hole, and m_0 is the mass of an electron),[46] q_e is the elementary charge (1.6×10^{-19} C), and ε_0 is the free space permittivity. From eq 3, the N_e value in the Au domain was estimated to be in the range of (1.50−1.68) $\times 10^{22}$ cm^{-3}, and the N_h value in the $Cu_{2-x}Se$ domain is in the range of (3.83−4.45) $\times 10^{21}$ cm^{-3}; both N_e and N_h decrease with the increase of the $Cu_{2-x}Se$:Au molar ratio from 0.18 to 3.77 (Table 1). The N_e value of all Au@$Cu_{2-x}Se$ nanocrescents is slightly lower than 1.87×10^{22} cm^{-3} of the AuNPs, but their N_h values are much higher than 4.05×10^{21} cm^{-3} of the $Cu_{2-x}Se$ NCs except the nanocrescent of the $Cu_{2-x}Se$:Au molar ratio of 3.77. The present Au@$Cu_{2-x}Se$ nanocrescents were made with the fixed Au domain size and the varied $Cu_{2-x}Se$ domain size. The "x" value representing the degree of Cu deficiency in $Cu_{2-x}Se$ nanoparticles is proportional to the free hole density; previous studies showed the insensitivity of the SPR wavelength of $Cu_{2-x}Se$ nanoparticles to the particulate size. As shown in Table 1, all Au@$Cu_{2-x}Se$ nanocrescents possess the similar "x" value of 0.2, which cannot explain the different free hole densities among these nanocrescents. We attribute the different hole densities to the interplay between the Au domain and the $Cu_{2-x}Se$ domain due to the varied $Cu_{2-x}Se$ domain size.

TA spectra have been widely used to study the carrier dynamics, and the carrier−phonon and phonon−phonon interactions in plasmonic noble metals, but few efforts have been devoted to examine the dynamics of charge carriers in the Au−$Cu_{2-x}Se$ hybrid system. Here, we performed TA studies to gain insights into the carrier dynamics in the Au@$Cu_{2-x}Se$ nanocrescents pumped with a 100 fs pulse laser at 380 and 800 nm, respectively (Figure 5). Because the threshold energy of

DOI: 10.1021/acs.chemmater.9b04100
Chem. Mater. 2019, 31, 9875−9886

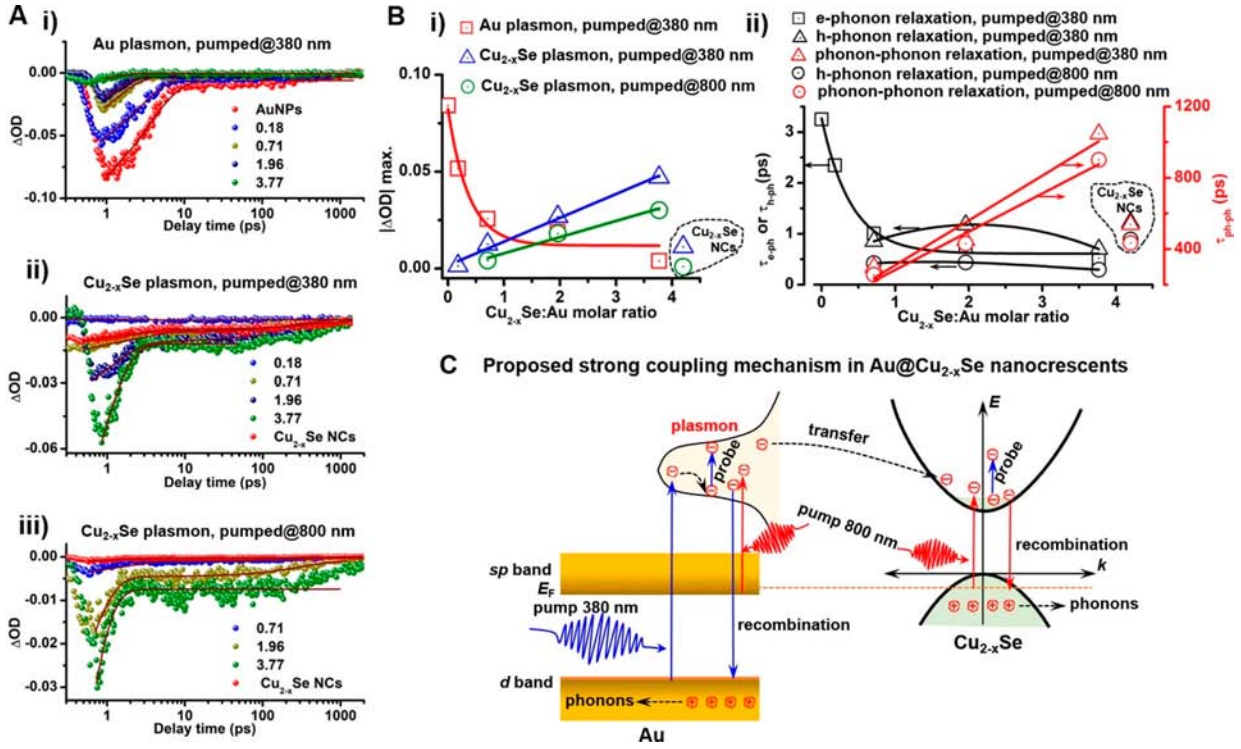

Figure 6. $Cu_{2-x}Se$:Au molar ratio-dependent bleaching dynamics and proposed coupling mechanism in Au@$Cu_{2-x}Se$ nanocrescents. (A) Bleaching dynamics of the TA signal (i) of the intrinsic SPR of AuNPs and the Au domain in Au@$Cu_{2-x}Se$ nanocrescents of various $Cu_{2-x}Se$:Au molar ratios pumped at 380 nm, and (ii, iii) of the intrinsic NIR SPR of $Cu_{2-x}Se$ NCs and the $Cu_{2-x}Se$ domain in Au@$Cu_{2-x}Se$ nanocrescents of various $Cu_{2-x}Se$:Au molar ratios pumped at (ii) 380 nm and (iii) 800 nm. (B) Effects of $Cu_{2-x}Se$:Au molar ratio on (i) the bleaching amplitude and (ii) electron/hole/photon−photon relaxation time constant at the SPR wavelengths of the Au and $Cu_{2-x}Se$ domains pumped at 380 and 800 nm, respectively. Results of AuNPs and $Cu_{2-x}Se$ NCs are shown as well. (C) Schematic illustrating the proposed coupling mechanism in the dual-plasmonic Au@$Cu_{2-x}Se$ nanocrescents.

the interband transition in AuNPs is ∼2.4 eV (∼520 nm), the pulse laser of 380 nm is able to trigger its interband transition from 5d-band to the hybridized 6sp-band, resulting in a transient increase in both hole density in the 5d-band and electron density in the 6sp-band.[47] With the excitation of 380 nm-pulse laser, the TA spectra of AuNPs exhibit a negative bleaching band at ∼528 nm and two positive absorption bands centered at 480 and 565 nm, respectively (Figure 5A). The negative TA signal is due to the "bleaching" of the intrinsic Au SPR band; the positive TA signals at 480 and 565 nm are due to the thermal broadening of the SPR band resulting from an increase in the electronic temperature induced by the pulse laser excitation.[48] The TA spectra of $Cu_{2-x}Se$ NCs show a broad negative band located in the NIR (900−1100 nm) region originating from the bleaching of the intrinsic NIR SPR of $Cu_{2-x}Se$ NCs, observable under the 380 nm- or 800 nm-pulse laser. Previous studies suggested that, with the excitation of the pulse laser, $Cu_{2-x}Se$ NCs followed bleaching behaviors of plasmonic electrons similar to those in noble metal (Au and Ag) nanoparticles.[21] Time-resolved TA spectra show the gradual decrease of the TA signals of the intrinsic SPRs of AuNPs and $Cu_{2-x}Se$ NCs for both 380 nm- and 800 nm-pulse lasers (Figure 5A,B). In addition, we found that the intrinsic TA signal of $Cu_{2-x}Se$ NCs under the 800 nm-pulse laser was much lower than that under the 380 nm-pulse laser, indicating the additional contribution from the resonant excitation with the 380 nm-pulse laser. Similarly, both positive and negative TA bands of the Au domain of the Au@$Cu_{2-x}Se$ nanocrescent with the $Cu_{2-x}Se$:Au molar ratio of 0.71 weaken over delay time as well, but their TA signals are much weaker than those of AuNPs (Figure 5C). In addition, we surprisingly found that the intrinsic TA signal of its $Cu_{2-x}Se$ domain was much stronger in the Au@$Cu_{2-x}Se$ nanocrescents than that in $Cu_{2-x}Se$ NCs under both 380 and 800 nm pulse lasers. This indicates the enhanced NIR optical absorption due to the electronic interplay between the plasmonic Au and $Cu_{2-x}Se$ domains of the Au@$Cu_{2-x}Se$ nanocrescent.

We further examined the bleaching dynamics of the intrinsic TA signals of Au@$Cu_{2-x}Se$ nanocrescents of different $Cu_{2-x}Se$:Au molar ratios (Figure 6A,B). The excitation with the pulse laser creates a nonthermal distribution of charge carriers (electrons in the Au domain and holes in the $Cu_{2-x}Se$ domain) and accordingly causes an increase in the carrier temperature, producing a thermalized electron gas (hot electrons) with higher temperature than the lattices.[21,49,50] The newly generated distribution of carriers can be reached on a time scale of subpicosecond via strong carrier−carrier scattering, followed by the bleaching of the SPR bands through fast carrier−phonon coupling within few picoseconds and slow phonon−phonon coupling within a few hundred picoseconds. It can be seen that the bleaching amplitude of the intrinsic TA signal of the Au domain exponentially decreases with the increase of the $Cu_{2-x}Se$:Au molar ratio under the excitation of 380 nm-pulse laser, while the bleaching amplitude of the intrinsic TA signal of the $Cu_{2-x}Se$ domain linearly increases with the increasing $Cu_{2-x}Se$:Au molar ratio under both 380 nm- and 800 nm-pulse lasers, except the Au@$Cu_{2-x}Se$ nanocrescent with the $Cu_{2-x}Se$:Au molar ratio of 0.18

DOI: 10.1021/acs.chemmater.9b04100
Chem. Mater. 2019, 31, 9875−9886

due to the low loading (accordingly too weak NIR SPR absorption) of $Cu_{2-x}Se$ (Figure 6B(i)). It is worth noting that the bleaching amplitude of the TA signal of the $Cu_{2-x}Se$ SPR in the nanocrescents is much larger than the $Cu_{2-x}Se$ NCs over the $Cu_{2-x}Se$:Au molar ratio range of 0.71−3.77 regardless of the excitation of the 380 nm- or 800 nm-pulse laser. These results suggest the decreasing electron density in the Au domain due to the transfer of electrons from the Au domain to the $Cu_{2-x}Se$ domain; the increasing size of the $Cu_{2-x}Se$ domain could increase the NIR absorption cross-section and thus compensate the neutralization effect of electron transfer to the hole-rich $Cu_{2-x}Se$ domain, leading to an increase in the bleaching amplitude with the increasing $Cu_{2-x}Se$:Au molar ratio.

Furthermore, we found that the dynamic TA signal of the intrinsic SPR of Au followed a monoexponential decay over time, while the dynamic TA signal of the intrinsic SPR of $Cu_{2-x}Se$ showed a biexponential decay process (Figure 6A). Thus, the fast carrier−phonon scattering time constant (τ_{c-ph}) and the slow phonon−phonon relaxation time constant (τ_{ph-ph}) of Au@$Cu_{2-x}Se$ nanocrescents can be extracted from the function as follows:[48,51]

$$f(t) = A_f \exp\left(-\frac{t}{\tau_{c-ph}}\right) + A_s\left(-\frac{t}{\tau_{ph-ph}}\right) + A_0 \quad (4)$$

where the first term corresponds to the carrier−phonon scattering process, and the second term and the constant term (A_0) represent the phonon−phonon relaxation process; A_f and A_s are the corresponding constant coefficients for the first and second terms, respectively. The fitting of the dynamic TA curve was performed in the range from the delay time with the SPR bleaching maximum to the delay time when the TA signal is almost constant over time. The electron−phonon scattering time constant (τ_{e-ph}) and hole−phonon scattering time constant (τ_{h-ph}) can be obtained from the dynamic curves of the TA signals of the SPRs of Au and $Cu_{2-x}Se$, respectively. Because $Cu_{2-x}Se$ has a carrier behavior similar to that of noble metals,[21,49] we assume that the relaxation processes of excited carriers in $Cu_{2-x}Se$ have the same physical origin as those of noble metals. Thus, we can achieve two time-constants from the fitting results and assign the small and large time-constants as the τ_{c-ph} and τ_{ph-ph}, respectively. The monoexponential decay of the TA signal of the Au SPR indicates the constant phonon−phonon relaxation time constant involved in the constant term (A_0).[51] Results show that the τ_{e-ph} value exponentially decreases with the increasing $Cu_{2-x}Se$:Au molar ratio, and becomes almost constant when the $Cu_{2-x}Se$:Au molar ratio exceeds 0.71; the τ_{h-ph} value that varies insignificantly with the $Cu_{2-x}Se$:Au molar ratio is much larger under the 380 nm-pulse laser than that under the 800 nm-pulse laser over the $Cu_{2-x}Se$:Au ratio range of 0.71−3.77. In addition, the hole−phonon relaxation of the $Cu_{2-x}Se$ SPR in the nanocrescents is much faster than $Cu_{2-x}Se$ NCs over the $Cu_{2-x}Se$:Au molar ratio range of 0.71−3.77 under both 380 nm- and 800 nm-pulse lasers. The τ_{ph-ph} value linearly increases with the increase of the $Cu_{2-x}Se$:Au molar ratio over the range investigated for both 380 nm- and 800 nm-pulse lasers. The τ_{ph-ph} value of $Cu_{2-x}Se$ NCs is much larger than those of the nanocrescents with the $Cu_{2-x}Se$:Au molar ratio of 0.71 and 1.96, but smaller than that of the nanocrescents with the $Cu_{2-x}Se$:Au molar ratio of 3.77, regardless of the 380 nm- or 800 nm-pulse laser. Unfortunately, we were unable to obtain the τ_{h-ph} and τ_{ph-ph} values for Au@$Cu_{2-x}Se$ nanocrescents of a $Cu_{2-x}Se$:Au molar ratio of less than 0.71 because of the low TA signal of the intrinsic SPR of $Cu_{2-x}Se$. It is worth noting that both bleaching amplitude and τ_{e-ph} of the Au SPR follow the similar change trend with the $Cu_{2-x}Se$:Au molar ratio. The rationale is that the electron transfer from the Au domain to the $Cu_{2-x}Se$ domain decreases electron density and thus accelerates the electron−phonon relaxation in the Au domain. Similarly, both the bleaching amplitude of the $Cu_{2-x}Se$ SPR and the phonon−phonon relaxation time-constant increase with the $Cu_{2-x}Se$:Au molar ratio. The electron transfer from the Au domain to the $Cu_{2-x}Se$ domain decreases the hole density in the $Cu_{2-x}Se$ domain, but the increasing $Cu_{2-x}Se$ domain size results in the increase of the extinction cross-section of the NIR SPR band, which slows the phonon−phonon relaxation process.

On the basis of the aforementioned analysis, we propose a possible mechanism that elucidates the interactions between the Au and $Cu_{2-x}Se$ domains of the Au@$Cu_{2-x}Se$ nanocrescents, schematically illustrated in Figure 6C. Both interband transition and SPR excitation would induce the generation of hot electrons, which could subsequently transfer from the Au domain to the $Cu_{2-x}Se$ domain. The increasing $Cu_{2-x}Se$ domain size enhances the extraction of hot electrons from the Au domain, which decreases the electron density in the Au domain. Despite the charge neutralization in the $Cu_{2-x}Se$ domain, the increasing $Cu_{2-x}Se$ size causes the increase of the NIR extinction cross-section and thereby increases the bleaching amplitude of the TA signal of the intrinsic SPR of $Cu_{2-x}Se$. The hot electrons and holes transfer to the surrounding lattices through the electron−phonon and hole−phonon interactions, which enhance the phonon−phonon relaxation process, and weaken both the electron−phonon scattering in the Au domain and the hole−phonon scattering in the $Cu_{2-x}Se$ domain of the nanocrescents. Therefore, this work presents new physical insights into the coupling interactions existing in the Au@$Cu_{2-x}Se$ nanocrescents, and thereby an in-depth understanding of their optical properties, benefiting the design of Au−$Cu_{2-x}Se$ hybrids of optimal optical properties for a diversity of plasmon-based applications.

CONCLUSIONS

In summary, a selenium-mediated two-step synthetic approach has been developed to prepare high-quality dual-plasmonic Au@$Cu_{2-x}Se$ nanocrescents, which allows tuning the $Cu_{2-x}Se$ domain size and the plasmonic properties in the NIR-II region by changing the concentration of the SeO_2 precursor. $Cu_{2-x}Se$ grows unidirectionally on the Au core with more addition of the SeO_2 precursor, forming the asymmetric crescent structure responsible for the unique plasmonic properties of Au@$Cu_{2-x}Se$ nanocrescents. The Au@$Cu_{2-x}Se$ nanocrescents exhibit two characteristic SPR bands positioned at the visible and NIR-II regions that originate from the collective oscillation of free electrons and free holes in the Au and $Cu_{2-x}Se$ domains of the nanocrescents, respectively. With the increasing $Cu_{2-x}Se$ domain size, the NIR SPR band of the $Cu_{2-x}Se$ domain becomes more intense with a slight red-shift. The theoretical modeling shows the asymmetric electric field distributions arising from the asymmetric structure of the nanocrescents. Both experimental results and theoretical calculation confirm the strong coupling between the Au and $Cu_{2-x}Se$ domains of the nanocrescents, accounting for their enhanced optical

DOI: 10.1021/acs.chemmater.9b04100
Chem. Mater. 2019, 31, 9875−9886

properties with respect to AuNPs and $Cu_{2-x}Se$ NCs. TA measurements suggest the $Cu_{2-x}Se$ domain size-dependent bleaching amplitude and carrier dynamics of the intrinsic SPRs corresponding to the Au and $Cu_{2-x}Se$ domains with variations of the carrier−phonon and phonon−phonon coupling interactions. A coupling mechanism between the Au and $Cu_{2-x}Se$ domains of the nanocrescents is proposed to explain the $Cu_{2-x}Se$-dependent plasmonic properties. This work presents not only a synthetic method for the high-quality dual-plasmonic Au@$Cu_{2-x}Se$ nanocrescents but also generates new physical insights into the interplay between their Au and $Cu_{2-x}Se$ domains. We foresee a huge potential of this type of dual-plasmonic hybrids for NIR-II plasmonic applications in photovoltaics, photocatalysis, and biomedicine.

MATERIALS AND METHODS

Chemicals and Materials. All chemicals and solvents were of analytical grade and used as received unless otherwise specified. Sodium borohydride ($NaBH_4$, >98%), copper(II) sulfate pentahydrate ($CuSO_4·5H_2O$, ≥99%), ascorbic acid (Vc, ≥99%), and selenium dioxide (SeO_2, ≥99%) were obtained from Sinopharm Chemical Reagent Co., Ltd. Chloroauric acid ($HAuCl_4·4H_2O$, 99% trace metals basis) was ordered from Shanghai Civi Chemical Technology Co., Ltd. Hexadecyltrimethylammonium chloride (CTAC, 97%) was purchased from Aladdin Chemistry Co., Ltd. Gold standard solution (1000 μg/mL) containing 1.5 M HCl, copper standard solution (1000 μg/mL) containing 1.0 M HNO_3, and selenium standard solution (1000 μg/mL) containing 2.0 M HNO_3 were obtained from Guobiao (Beijing) Testing and Certification Co., Ltd. Ultrapure water with a resistivity of 18.2 MΩ cm (at 25 °C) was produced with a Millipore Direct-Q3 UV system (Molshein, France) and used in the entire experiment. All glassware used in this work was cleaned with aqua regia, rinsed thoroughly with ultrapure water, and then air-dried prior to use throughout all experiments.

Synthesis of Au Nanoparticles (AuNPs). The spherical AuNPs were synthesized according to the well-established protocol described in the literature.[52] First, 0.3 mL of 10 mM ice-cold $NaBH_4$ aqueous solution was added to a solution containing 2.5 mL of 0.15 M CTAC solution and 0.025 mL of 50 mM $HAuCl_4$. After being vigorously stirred for 2 min, the solution was kept still at room temperature for 1 h, producing the Au seed solution. Next, 3.2 mL of 0.2 M CTAC solution was mixed with 0.8 mL of 10 mM $HAuCl_4$ solution at room temperature, followed by successive addition of 35 mL of ultrapure water and 3.8 mL of 0.1 M Vc solution under gentle stirring, producing the growth solution. Ten microliters of the Au seed solution was added to the growth solution at room temperature. After being vigorously shaken for 1 min, the reaction solution was aged at 30 °C for at least 8 h. Finally, the reaction solution was centrifuged at 7500 rpm, and the pellet was the AuNP products with an optical extinction peak of 524 nm, which were dispersed in ultrapure water with a final concentration of 2.0 nM for further use.

Synthesis of $Cu_{2-x}Se$ Nanocrystals. 200 μL of 0.1 M Vc aqueous solution was added into 3 mL of 20 mM CTAC aqueous solution followed by the addition of SeO_2 with a final concentration of 2.44 mM. After being stirred for 10 min, a freshly prepared mixture consisting of 80 μL of 0.2 M $CuSO_4·5H_2O$ and 0.4 mL of 0.1 M Vc aqueous solution was added under vigorous stirring. The reaction was allowed to continue until a dark green solution was observed, indicating the formation of $Cu_{2-x}Se$ NCs.

Synthesis of Au@$Cu_{2-x}Se$ Nanocrescents. Two milliliters of the 20 mM CTAC aqueous solution was added to 1 mL of 2.0 nM AuNP suspension under vigorous stirring at 30 °C. Next, 200 μL of 0.1 M Vc aqueous solution was added, followed by the addition of a given amount of SeO_2 aqueous solution to get a final SeO_2 concentration of 0.083, 0.33, 1.00, 1.33, or 2.00 mM. After being stirred for 10 min, a solution containing 30 μL of 0.2 M $CuSO_4·5H_2O$ and 0.4 mL of 0.1 M Vc aqueous solution was added. The mixture was allowed to react under vigorous stirring at room temperature for overnight. The resulting products were purified by successive centrifugation and washing, and then redispersed in 1 mL of ultrapure water for further use.

Characterization and Instrumentation. Transmission electron microscopy (TEM) images were taken using an FEI Tecnai G2 F20 transmission electron microscope (FEI, U.S.) operating at 200 kV; high-resolution TEM (HRTEM) images, high-angle annular dark-field scanning TEM (HAADF-STEM) images, and energy dispersive X-ray (EDX) elemental mapping were obtained on an FEI Titan G2 80-200 transmission electron microscope equipped with a spherical aberration corrector, allowing it to reach a spatial resolution of ∼0.7 Å at 300 kV. The geometric parameters of all samples were measured from the TEM data using the ImageJ analysis software. At least 100 nanoparticles were counted for each type of sample, and Gaussian fitting was carried out to obtain the average size of nanoparticles. UV−vis−NIR extinction spectra were measured in the wavelength range from 175 to 3300 nm using a Cary 5000 UV−vis−NIR spectrophotometer (Agilent Technology, U.S.). The crystal structures were determined by a SmartLab3 kW X-ray diffractometer (Rigaku, Japan) using Cu Kα radiation (λ = 1.5406 Å) operating at 40 kV and 30 mA. The elemental composition of samples was measured by inductively coupled plasma-optical emission spectroscopy (ICP-OES) on an Agilent 5100 inductively coupled plasma−optical emission spectrometer (Agilent Technologies, U.S.). Samples for the ICP-OES measurements were digested in concentrated nitric acid, followed by dilution with ultrapure water.

Transient Absorption Measurements. The TA measurements were performed at room temperature on the ExciPro femtosecond pump−probe system (CDP Systems Corp.), equipped with a regeneratively amplified Ti:sapphire ultrafast laser system for the excitation (Coherent Astrella).[53,54] The incident pump pulses with the wavelength of 380/800 nm and pulse width of 100 fs were generated by an ultrafast optical parametric amplifier (Coherent OperA Solo). The probe beams were produced from a thin CaF_2 plate, which were focused into a fiber-coupled multichannel spectrometer with complementary metal oxide semiconductor sensors at a frequency of 1 kHz. The power of the pump pulses was adjustable with a series of neutral density filter wheels. The delay between the pump and probe pulses was controlled by a motorized delay stage. The TA spectra and dynamic data were collected over a broad spectral range in a transmission mode with a 0.3 mW pump power and a ∼300 μm focused spot size of pumping beam on the aqueous suspension of samples, which were placed in a 10 mm-thick quartz cuvette. The concentration of the samples was controlled to have the same power density for the excitation, which allows for the comparison of the bleaching amplitude between samples.

Theoretical Modeling of the Plasmonic Properties. Both extinction spectra and electric field distribution were calculated by the Finite-Difference Time-Domain (FDTD) method using the commercial software Lumerical FDTD Solutions 8.19.1584 (Lumerical Solutions, Inc., Canada). For the simplicity of Au@$Cu_{2-x}Se$ nanocrescents, we modeled an AuNP core with a sphere of 25 nm in diameter, conformally coated with a 2 nm-thick $Cu_{2-x}Se$ layer and then deposited with an additional asymmetric $Cu_{2-x}Se$ shell of various sizes, schematically shown in Figure S2. The dimensional parameters of the Au and $Cu_{2-x}Se$ domains were statistically measured from the TEM data and used for the model creation. The dielectric function of Au was taken from the measured data by Johnson and Christy,[55] while the dielectric function ($\varepsilon(\omega) = \varepsilon_1(\omega) + i\varepsilon_2(\omega)$) of $Cu_{2-x}Se$ with various $Cu_{2-x}Se$ domain sizes was calculated by the Drude model:[18,44,45]

$$\varepsilon_1 = \varepsilon_\infty - \frac{\omega_p^2}{\omega^2 + \gamma^2} \tag{5}$$

$$\varepsilon_2 = \frac{\omega_p^2 \gamma}{\omega(\omega^2 + \gamma^2)} \tag{6}$$

where ε_∞ is the high frequency dielectric permittivity, and ω_p and γ are the plasma frequency of free carriers of the nanoparticles and the

DOI: 10.1021/acs.chemmater.9b04100
Chem. Mater. 2019, 31, 9875−9886

free carrier damping, respectively. The background dielectric constant ε_∞ is due to the presence of interband transitions at higher photon energy, for example, $\varepsilon_\infty = 1$ for Au, $\varepsilon_\infty = 7$ for $Cu_{2-x}Se$ at $x \approx 0.2$.[46] The background refractive index of the surrounding medium (water) was set to be 1.33. A total-field scattered-field was employed as the incident source for calculations of both electric field distribution and extinction spectra in the wavelength range from 400 to 2000 nm. The mesh size of the box containing a geometric structure was set as 0.25 nm. The calculated extinction cross-section (σ_{theory}) from the FDTD simulations was converted to the theoretical molar extinction coefficients (ε_{theory}) by the following equation:[56]

$$\varepsilon_{theory} = \frac{N_A}{2.3 \times 10^3} \cdot \sigma_{theory} \ (M^{-1}\ cm^{-1}) \quad (7)$$

()where N_A is Avogadro's number.

■ ASSOCIATED CONTENT

Supporting Information

The Supporting Information is available free of charge at https://pubs.acs.org/doi/10.1021/acs.chemmater.9b04100.

Calculation of the concentration of the particulate size of nanoparticles, unit cell structures of cubic Au and cubic berzelianite $Cu_{2-x}Se$, crystallographic parameters of the unit cells of cubic Au and cubic berzelianite $Cu_{2-x}Se$, schematic of the model of the Au@$Cu_{2-x}Se$ nanocrescents for the FDTD simulations, TEM image and size distribution of as-synthesized $Cu_{2-x}Se$ NCs, size distribution of Au@$Cu_{2-x}Se$ nanocrescents, and the $Cu_{2-x}Se$ domain size-dependent electric field ($\log|E|^2/|E_0|^2$) distributions at the calculated SPR wavelengths corresponding to the Au and $Cu_{2-x}Se$ domains (PDF)

■ AUTHOR INFORMATION

Corresponding Authors

*E-mail: liming0823@gmail.com, liming0823@csu.edu.cn.
*E-mail: chenr@sustech.edu.cn.

ORCID

Rui Chen: 0000-0002-0445-7847
Ming Li: 0000-0002-2289-0222

Notes

The authors declare no competing financial interest.

■ ACKNOWLEDGMENTS

We would like to acknowledge financial support by the National Natural Science Foundation of China (Grants 51871246 and 11574130), the Innovation-Driven Project of Central South University (Grant 2018CX002) and Hunan Provincial Science & Technology Program (Grant 2017XK2027), and the Shenzhen Science and Technology Innovation Commission (Grants KQJSCX20170726145748464 and JCYJ20180305180553701).

■ REFERENCES

(1) Zhang, Y.; He, S.; Guo, W.; Hu, Y.; Huang, J.; Mulcahy, J. R.; Wei, W. D. Surface-plasmon-driven hot electron photochemistry. *Chem. Rev.* **2018**, *118* (6), 2927−2954.
(2) Shan, B.; Pu, Y.; Chen, Y.; Liao, M.; Li, M. Novel SERS labels: rational design, functional integration and biomedical applications. *Coord. Chem. Rev.* **2018**, *371*, 11−37.
(3) Li, M.; Cushing, S. K.; Wu, N. Plasmon-enhanced optical sensors: a review. *Analyst* **2015**, *140* (2), 386−406.
(4) Zhou, L.; Swearer, D. F.; Zhang, C.; Robatjazi, H.; Zhao, H.; Henderson, L.; Dong, L.; Christopher, P.; Carter, E. A.; Nordlander, P.; Halas, N. J. Quantifying hot carrier and thermal contributions in plasmonic photocatalysis. *Science* **2018**, *362* (6410), 69−72.
(5) Rycenga, M.; Cobley, C. M.; Zeng, J.; Li, W.; Moran, C. H.; Zhang, Q.; Qin, D.; Xia, Y. Controlling the synthesis and assembly of silver nanostructures for plasmonic applications. *Chem. Rev.* **2011**, *111* (6), 3669−3712.
(6) Zhou, W.; Gao, X.; Liu, D.; Chen, X. Gold nanoparticles for in vitro diagnostics. *Chem. Rev.* **2015**, *115* (19), 10575−10636.
(7) Kriegel, I.; Scotognella, F.; Manna, L. Plasmonic doped semiconductor nanocrystals: Properties, fabrication, applications and perspectives. *Phys. Rep.* **2017**, *674*, 1−52.
(8) Pradhan, N.; Das Adhikari, S.; Nag, A.; Sarma, D. D. Luminescence, plasmonic, and magnetic properties of doped semiconductor nanocrystals. *Angew. Chem., Int. Ed.* **2017**, *56* (25), 7038−7054.
(9) Zhao, Y.; Pan, H.; Lou, Y.; Qiu, X.; Zhu, J.; Burda, C. Plasmonic $Cu_{2-x}S$ nanocrystals: optical and structural properties of copper-deficient copper (I) sulfides. *J. Am. Chem. Soc.* **2009**, *131* (12), 4253−4261.
(10) González-Rubio, G.; Díaz-Núñez, P.; Rivera, A.; Prada, A.; Tardajos, G.; González-Izquierdo, J.; Bañares, L.; Llombart, P.; Macdowell, L. G.; Palafox, M. A.; Liz-Marzán, L. M. Femtosecond laser reshaping yields gold nanorods with ultranarrow surface plasmon resonances. *Science* **2017**, *358* (6363), 640−644.
(11) Alvarez, M. M.; Khoury, J. T.; Schaaff, T. G.; Shafigullin, M. N.; Vezmar, I.; Whetten, R. L. Optical absorption spectra of nanocrystal gold molecules. *J. Phys. Chem. B* **1997**, *101* (19), 3706−3712.
(12) Schwartzberg, A. M.; Olson, T. Y.; Talley, C. E.; Zhang, J. Z. Synthesis, characterization, and tunable optical properties of hollow gold nanospheres. *J. Phys. Chem. B* **2006**, *110* (40), 19935−19944.
(13) Gallinet, B.; Martin, O. J. Refractive index sensing with subradiant modes: a framework to reduce losses in plasmonic nanostructures. *ACS Nano* **2013**, *7* (8), 6978−6987.
(14) Li, M.; Cushing, S. K.; Zhang, J.; Lankford, J.; Aguilar, Z. P.; Ma, D.; Wu, N. Shape-dependent surface-enhanced Raman scattering in gold−Raman-probe−silica sandwiched nanoparticles for biocompatible applications. *Nanotechnology* **2012**, *23*, 115501.
(15) Zhang, Q.; Hu, Y.; Guo, S.; Goebl, J.; Yin, Y. Seeded growth of uniform Ag nanoplates with high aspect ratio and widely tunable surface plasmon bands. *Nano Lett.* **2010**, *10* (12), 5037−5042.
(16) Gole, A.; Murphy, C. J. Seed-mediated synthesis of gold nanorods: role of the size and nature of the seed. *Chem. Mater.* **2004**, *16* (19), 3633−3640.
(17) Huang, J.; Guo, M.; Ke, H.; Zong, C.; Ren, B.; Liu, G.; Shen, H.; Ma, Y.; Wang, X.; Zhang, H.; Deng, Z. Rational design and synthesis of γFe_2O_3@ Au magnetic gold nanoflowers for efficient cancer theranostics. *Adv. Mater.* **2015**, *27* (34), 5049−5056.
(18) Luther, J. M.; Jain, P. K.; Ewers, T.; Alivisatos, A. P. Localized surface plasmon resonances arising from free carriers in doped quantum dots. *Nat. Mater.* **2011**, *10* (5), 361−366.
(19) Agrawal, A.; Cho, S. H.; Zandi, O.; Ghosh, S.; Johns, R. W.; Milliron, D. J. Localized surface plasmon resonance in semiconductor nanocrystals. *Chem. Rev.* **2018**, *118* (6), 3121−3207.
(20) Dorfs, D.; Härtling, T.; Miszta, K.; Bigall, N. C.; Kim, M. R.; Genovese, A.; Falqui, A.; Povia, M.; Manna, L. Reversible tunability of the near-infrared valence band plasmon resonance in $Cu_{2-x}Se$ nanocrystals. *J. Am. Chem. Soc.* **2011**, *133* (29), 11175−11180.
(21) Kriegel, I.; Jiang, C.; Rodríguez-Fernández, J.; Schaller, R. D.; Talapin, D. V.; Da Como, E.; Feldmann, J. Tuning the excitonic and plasmonic properties of copper chalcogenide nanocrystals. *J. Am. Chem. Soc.* **2012**, *134* (3), 1583−1590.
(22) Ou, W.; Zou, Y.; Wang, K.; Gong, W.; Pei, R.; Chen, L.; Pan, Z.; Fu, D.; Huang, X.; Zhao, Y.; Lu, W. Active manipulation of NIR plasmonics: the case of $Cu_{2-x}Se$ through electrochemistry. *J. Phys. Chem. Lett.* **2018**, *9* (2), 274−280.
(23) Cui, J.; Jiang, R.; Guo, C.; Bai, X.; Xu, S.; Wang, L. Fluorine Grafted Cu_7S_4−Au heterodimers for multimodal imaging guided

DOI: 10.1021/acs.chemmater.9b04100
Chem. Mater. 2019, 31, 9875−9886

photothermal therapy with high penetration depth. *J. Am. Chem. Soc.* **2018**, *140* (18), 5890−5894.
(24) Wang, X.; Liow, C.; Bisht, A.; Liu, X.; Sum, T. C.; Chen, X.; Li, S. Engineering interfacial photo-induced charge transfer based on nanobamboo array architecture for efficient solar-to-chemical energy conversion. *Adv. Mater.* **2015**, *27* (13), 2207−2214.
(25) Chen, K.; Shinjo, S.; Sakuda, A.; Yamamoto, K.; Uchiyama, T.; Kuratani, K.; Takeuchi, T.; Orikasa, Y.; Hayashi, A.; Tatsumisago, M.; Kimura, Y.; Nakamura, T.; Amezawa, K.; Uchimoto, Y. Morphological effect on reaction distribution influenced by binder materials in composite electrodes for sheet-type all-solid-state lithium-ion batteries with sulfide-based solid electrolyte. *J. Phys. Chem. C* **2019**, *123*, 3292−3298.
(26) Liu, X.; Lee, C.; Law, W. C.; Zhu, D.; Liu, M.; Jeon, M.; Kim, J.; Prasad, P. N.; Kim, C.; Swihart, M. T. Au−Cu_{2-x}Se heterodimer nanoparticles with broad localized surface plasmon resonance as contrast agents for deep tissue imaging. *Nano Lett.* **2013**, *13* (9), 4333−4339.
(27) Maddinedi, S. B. Green synthesis of Au−Cu_{2-x}Se heterodimer nanoparticles and their in-vitro cytotoxicity, photothermal assay. *Environ. Toxicol. Pharmacol.* **2017**, *53*, 29−33.
(28) Ji, M.; Xu, M.; Zhang, W.; Yang, Z.; Huang, L.; Liu, J.; Zhang, Y.; Gu, L.; Yu, Y.; Hao, W.; An, P.; Zheng, L.; Zhu, H.; Zhang, J. Structurally well-defined Au@Cu_{2-x}S core−shell nanocrystals for improved cancer treatment based on enhanced photothermal efficiency. *Adv. Mater.* **2016**, *28* (16), 3094−3101.
(29) Lv, Q.; Min, H.; Duan, D. B.; Fang, W.; Pan, G. M.; Shen, A. G.; Wang, Q. Q.; Nie, G.; Hu, J. M. Total aqueous synthesis of Au@ Cu_{2-x}S core−shell nanoparticles for in vitro and in vivo SERS/PA imaging-guided photothermal cancer therapy. *Adv. Healthcare Mater.* **2018**, *8* (2), 1801257.
(30) Jiang, R.; Li, B.; Fang, C.; Wang, J. Metal/semiconductor hybrid nanostructures for plasmon-enhanced applications. *Adv. Mater.* **2014**, *26* (31), 5274−5309.
(31) Zou, Y.; Sun, C.; Gong, W.; Yang, X.; Huang, X.; Yang, T.; Lu, W.; Jiang, J. Morphology-controlled synthesis of hybrid nanocrystals via a selenium-mediated strategy with ligand shielding effect: the case of dual plasmonic Au−Cu_{2-x}Se. *ACS Nano* **2017**, *11* (4), 3776−3785.
(32) Ding, X.; Liow, C. H.; Zhang, M.; Huang, R.; Li, C.; Shen, H.; Liu, M.; Zou, Y.; Gao, N.; Zhang, Z.; Li, Y. Surface plasmon resonance enhanced light absorption and photothermal therapy in the second near-infrared window. *J. Am. Chem. Soc.* **2014**, *136* (44), 15684−15693.
(33) Kim, Y.; Park, K. Y.; Jang, D. M.; Song, Y. M.; Kim, H. S.; Cho, Y. J.; Myung, Y.; Park, J. Synthesis of Au−Cu_2S core−shell nanocrystals and their photocatalytic and electrocatalytic activity. *J. Phys. Chem. C* **2010**, *114* (50), 22141−22146.
(34) Zhu, H.; Wang, Y.; Chen, C.; Ma, M.; Zeng, J.; Li, S.; Xia, Y.; Gao, M. Monodisperse dual plasmonic Au@ Cu_{2-x}E (E= S, Se) core@shell supraparticles: aqueous fabrication, multimodal imaging, and tumor therapy at in vivo level. *ACS Nano* **2017**, *11* (8), 8273−8281.
(35) Li, Y.; Pan, G.; Liu, Q.; Ma, L.; Xie, Y.; Zhou, L.; Hao, Z.; Wang, Q. Coupling resonances of surface plasmon in gold nanorod/ copper chalcogenide core−shell nanostructures and their enhanced photothermal effect. *ChemPhysChem* **2018**, *19* (15), 1852−1858.
(36) Mou, J.; Li, P.; Liu, C.; Xu, H.; Song, L.; Wang, J.; Zhang, K.; Chen, Y.; Shi, J.; Chen, H. Ultrasmall Cu_{2-x}S nanodots for highly efficient photoacoustic imaging-guided photothermal therapy. *Small* **2015**, *11* (19), 2275−2283.
(37) Huang, Q.; Zhang, S.; Zhang, H.; Han, Y.; Liu, H.; Ren, F.; Sun, Q.; Li, Z.; Gao, M. Boosting the radiosensitizing and photothermal performance of Cu_{2-x}Se nanocrystals for synergetic radiophotothermal therapy of orthotopic breast cancer. *ACS Nano* **2019**, *13* (2), 1342−1353.
(38) Zhang, J.; Tang, Y.; Lee, K.; Ouyang, M. Nonepitaxial growth of hybrid core-shell nanostructures with large lattice mismatches. *Science* **2010**, *327* (5973), 1634−1638.
(39) Zhang, J.; Tang, Y.; Lee, K.; Ouyang, M. Tailoring light−matter−spin interactions in colloidal hetero-nanostructures. *Nature* **2010**, *466* (7302), 91−95.
(40) Gampel, L.; Johnson, F. M. Index of refraction of single-crystal selenium. *J. Opt. Soc. Am.* **1969**, *59*, 72−73.
(41) Leiga, A. G. Optical properties of amorphous selenium in the vacuum ultraviolet. *J. Opt. Soc. Am.* **1968**, *58* (11), 1411−1445.
(42) Wu, X. J.; Huang, X.; Liu, J.; Li, H.; Yang, J.; Li, B.; Huang, W.; Zhang, H. Two-dimensional CuSe nanosheets with microscale lateral size: Synthesis and template-assisted phase transformation. *Angew. Chem., Int. Ed.* **2014**, *53* (20), 5083−5087.
(43) Pu, Y.; Zhao, Y.; Zheng, P.; Li, M. Elucidating the growth mechanism of plasmonic gold nanostars with tunable optical and photothermal properties. *Inorg. Chem.* **2018**, *57* (14), 8599−8607.
(44) Le Ru, E.; Etchegoin, P. *Principles of Surface-Enhanced Raman Spectroscopy and Related Plasmonic Effects*; Elsevier: Amsterdam, The Netherlands, 2008.
(45) Marbella, L. E.; Gan, X. Y.; Kaseman, D. C.; Millstone, J. E. Correlating carrier density and emergent plasmonic features in Cu_{2-x}Se nanoparticles. *Nano Lett.* **2017**, *17* (4), 2414−2419.
(46) Mansour, B. A.; Demian, S. E.; Zayed, H. A. Determination of the effective mass for highly degenerate copper selenide from reflectivity measurements. *J. Mater. Sci.: Mater. Electron.* **1992**, *3* (4), 249−252.
(47) Perner, M.; Bost, P.; Lemmer, U.; Von Plessen, G.; Feldmann, J.; Becker, U.; Mennig, M.; Schmitt, M.; Schmidt, H. Optically induced damping of the surface plasmon resonance in gold colloids. *Phys. Rev. Lett.* **1997**, *78* (11), 2192.
(48) Ahmadi, T. S.; Logunov, S. L.; El-Sayed, M. A. Picosecond dynamics of colloidal gold nanoparticles. *J. Phys. Chem.* **1996**, *100*, 8053−8056.
(49) Scotognella, F.; Della Valle, G.; Srimath Kandada, A. R.; Dorfs, D.; Zavelani-Rossi, M.; Conforti, M.; Miszta, K.; Comin, A.; Korobchevskaya, K.; Lanzani, G.; Manna, L. Plasmon dynamics in colloidal Cu_{2-x}Se nanocrystals. *Nano Lett.* **2011**, *11* (11), 4711−4717.
(50) Yu, K.; You, G.; Polavarapu, L.; Xu, Q. H. Bimetallic Au/Ag core−shell nanorods studied by ultrafast transient absorption spectroscopy under selective excitation. *J. Phys. Chem. C* **2011**, *115* (29), 14000−14005.
(51) Yu, K.; Polavarapu, L.; Xu, Q. H. Excitation wavelength and fluence dependent femtosecond transient absorption studies on electron dynamics of gold nanorods. *J. Phys. Chem. A* **2011**, *115*, 3820−3826.
(52) Chen, T.; Xu, M.; Ji, M.; Cheng, L.; Liu, J.; Zhang, B.; Zhang, J. Aqueous phase synthesis of Au@Ag_3AuX_2 (X= Se, Te) core/shell nanocrystals and their broad NIR photothermal conversion application. *CrystEngComm* **2016**, *18* (29), 5418−5422.
(53) Zhao, F.; Li, J.; Gao, X.; Qiu, X.; Lin, X.; He, T.; Chen, R. Comparison studies of the linear and nonlinear optical properties of $CsPbBr_xI_{3-x}$ nanocrystals: the influence of dimensionality and composition. *J. Phys. Chem. C* **2019**, *123* (14), 9538−9543.
(54) Li, Y.; Cheng, J.; Li, J.; Delville, M. H.; Tréguer-Delapierre, M.; He, T.; Chen, R.; Tang, Z. Ultrafast dynamics of photoexcited hot carrier generation and injection in AgNWs@TiO_2@GNS nanostructures. *J. Phys. Chem. C* **2018**, *122* (26), 14857−14864.
(55) Johnson, P. B.; Christy, R. W. Optical constants of the noble metals. *Phys. Rev. B* **1972**, *6*, 4370.
(56) Wang, H.; Pu, Y.; Shan, B.; Li, M. Combining experiments and theoretical modeling to interrogate the anisotropic growth and structure−plasmonic property relationships of gold nanostars. *Inorg. Chem.* **2019**, *58* (18), 12457−12466.

DOI: 10.1021/acs.chemmater.9b04100
Chem. Mater. 2019, 31, 9875−9886